

Electronic subbands in the a -LaAlO₃/KTaO₃ interface revealed by quantum oscillations in high magnetic fields

Km Rubi ^{1,*} Shengwei Zeng,² Femke Bangma ¹ Michel Goiran,³ A. Ariando ^{2,†} Walter Escoffier,³ and Uli Zeitler¹

¹*High Field Magnet Laboratory (HFML-EMFL) and Institute for Molecules and Materials, Radboud University, 6525 ED Nijmegen, The Netherlands*

²*Department of Physics, National University of Singapore, 117551 Singapore*

³*Laboratoire National des Champs Magnétiques Intenses (LNCMI-EMFL), Université de Toulouse, CNRS, INSA, UPS, 143 Avenue de Rangueil, 31400 Toulouse, France*



(Received 12 March 2021; revised 16 July 2021; accepted 12 August 2021; published 10 September 2021)

Investigating Shubnikov-de Haas (SdH) oscillations in high magnetic fields, we experimentally infer the electronic band structure of the quasi-two-dimensional electron gas (2DEG) at the ionic-liquid gated amorphous (a)-LaAlO₃/KTaO₃ interface. The angular dependence of SdH oscillations indicates a 2D confinement of a majority of electrons at the interface. However, additional SdH oscillations with an angle-independent frequency observed at high tilt angles indicate the coexistence of 3D charge carriers extending deep into the KTaO₃. The SdH oscillations measured in magnetic fields perpendicular to the interface show four frequencies corresponding to four 2D subbands with different effective masses ($0.20 m_e$ – $0.55 m_e$). The single-frequency oscillations originating from 3D electrons yields a larger effective mass of $\sim 0.70 m_e$. Overall, the inferred subbands are in good agreement with the theoretical calculations and angle-resolved photoemission spectroscopy studies on 2DEG at KTaO₃ surface.

DOI: [10.1103/PhysRevResearch.3.033234](https://doi.org/10.1103/PhysRevResearch.3.033234)

I. INTRODUCTION

Due to its fundamental complexity and potential applications in new-generation semiconductor and spintronic devices, the two-dimensional electron gas (2DEG) formed at the interface between two insulating transition metal oxides has triggered significant attention in the past decade [1–4]. The 2DEG at perovskite oxide interfaces with strong spin-orbit coupling was first discovered for LaAlO₃/SrTiO₃ (LAO/STO) heterointerface [5–7]. This interface exhibits several exceptional phenomena, for example, the coexistence of ferromagnetism and superconductivity [8,9] and sets up a benchmark for other perovskite oxide based interfaces. In recent years, the 2DEG of even higher mobility and stronger spin-orbit coupling with electrons originating from the Ta:5d orbitals has been revealed at interfaces based on KTaO₃ (KTO), a band insulator ($E_g \sim 3.6$ eV) and polar oxide [10–13]. Additionally, 2D-superconductivity with higher critical temperature has been reported at the KTO surface [14] and KTO-based interfaces [15,16] of high carrier densities ($n \gtrsim 5 \times 10^{13}$ cm⁻²).

From the perspective of electronic band structure, the KTO-based 2DEG is similar to the STO-2DEG where electrons primarily occupy t_{2g} orbitals of transition metal ions. More specifically, density functional theory (DFT) calculations for the LAO/KTO interface reveal a partial occupancy of d_{xy} , d_{xz} , and d_{yz} subbands arising from the t_{2g} orbitals of Ta:5d band, and a dominant electronic contribution of the low-lying d_{xy} subband [17,18]. Tight-binding calculations for the 2DEG at the KTO surface predict a strong mixing of d_{xy} , d_{xz} , and d_{yz} orbitals driven by spin-orbit coupling and a reconstruction of orbital symmetries of subbands [19]. These findings are experimentally supported by angle-resolved photoemission spectroscopy (ARPES) measurements on oxygen-deficient KTO surface, which mapped out parabolic and isotropic light ($m^* \sim 0.3m_e$) and heavy ($m^* \sim 0.7m_e$) subbands [19,20]. In addition, quantum transport experiments performed at $T = 2$ K and up to $B = 14$ T on a metallic KTO surface, where oxygen vacancies were induced through Ar⁺ irradiation, have revealed a single frequency Shubnikov-de Haas (SdH) oscillations assigned to heavy electrons subband ($m^* = 0.8m_e$) [21].

To fully resolve the SdH oscillations corresponding to the closely spaced subbands of KTO-based 2DEGs, we have performed magneto-transport measurements on the amorphous (a)-LAO/KTO interface in high magnetic fields (30 T continuous and 55 T pulsed). Since the large lattice constant of KTO restricts the epitaxial growth of a heterointerface, we create a conducting interface by growing an amorphous a -LAO thin film on KTO. High-mobility carriers are induced at the interface using ionic-liquid (IL) gating at room temperature as reported before for a -LAO/STO [22,23]. We measured two devices of different carrier densities, device-1

*rubi.km@ru.nl

†ariando@nus.edu.sg

($n = 1.7 \times 10^{13} \text{ cm}^{-2}$) and device-2 ($n = 1.1 \times 10^{13} \text{ cm}^{-2}$), in high magnetic fields. Large-amplitude SdH oscillations of several frequencies are observed for both devices. For an in-depth characterization of the SdH oscillations, we study their tilt-angle and temperature dependencies for device-1. The oscillations measured for different tilt-angles reveal the coexistence of 2D and 3D conduction channels. The analysis of temperature dependent SdH oscillations yields effective masses ranging from $m^* \approx 0.2 m_e$ to $0.55 m_e$ and, therefore, confirms the occupancy of light and heavy subbands. Moreover, a back-gate-dependent study on device-2 provides additional smaller amplitude and higher frequency oscillations, barely visible in the raw data, in the low-density regime.

II. EXPERIMENTAL DETAILS

Our *a*-LAO/KTO devices consist of 4 nm LAO thin film deposited on the patterned Hall bar on the surface of a 500- μm -thick KTO(001) substrate using pulsed laser deposition. During deposition, the substrate temperature was kept at 25°C and the oxygen partial pressure was $p_{O_2} \sim 10^{-4}$ mbar. Six-terminal Hall bars of width 50 μm and length 160 μm between the longitudinal voltage leads were fabricated by conventional photolithography technique using AlN films as a hard mask, see Figs. 1(a) and 1(c). The Hall bars were bonded with Al wires using an ultrasonic wire bonder. A silver-paint electrode, (G) in Fig. 1(a), not connected to the Hall-bar was used as a counter-electrode for ionic-liquid gating with N,N-diethyl-N-methyl-N-(2-methoxyethyl)ammonium bis(trifluoromethyl sulphonyl)imide (DEME-TFSI).

Simultaneous measurements of longitudinal and Hall resistance were carried out in high dc magnetic field ($B_{\text{max}} = 30 \text{ T}$) at HFML-Nijmegen and high pulsed magnetic field ($B_{\text{max}} = 55 \text{ T}$ with duration of 300 ms) at LNCMI-Toulouse. The dc-field measurements were performed in a ^3He system and a dilution refrigerator, and the pulsed field measurements in a ^3He system. For pulsed field measurements, we apply a dc current excitation of 5 μA , whereas we use a lower ac current of 100 nA for measurements in continuous fields. An *in situ* rotation mechanism was used to change the angle between magnetic field orientation and the normal direction of the interface.

III. RESULTS AND DISCUSSION

Figure 1(a) shows a top-view of the *a*-LAO/KTO device including a measurement scheme for the IL gating. A tiny drop of the IL covers the gate electrode and the conducting KTO channel. The source-drain current, I_{SD} is measured with varying IL gate voltage, V_g at a constant source-drain voltage, V_{SD} of 3 V, and we show the conductance ($G = I_{\text{SD}}/V_{\text{SD}}$) as a function of V_g in Fig. 1(b). The device switches from a high-conductance ($\sim 10^{-5} \text{ S}$) to a low-conductance ($\sim 10^{-10} \text{ S}$) state when V_g sweeps from +2 V to -6 V. A large hysteresis in $G(V_g)$ in the first scan cycle demonstrates an irreversible doping response, whereas the doping becomes almost reversible with a small hysteresis from the second cycle onwards. The onset of conduction and the hysteretic behavior can be explained by electromigration of oxygen ions from the *a*-LAO toward the interface thereby irreversibly filling oxygen vacan-

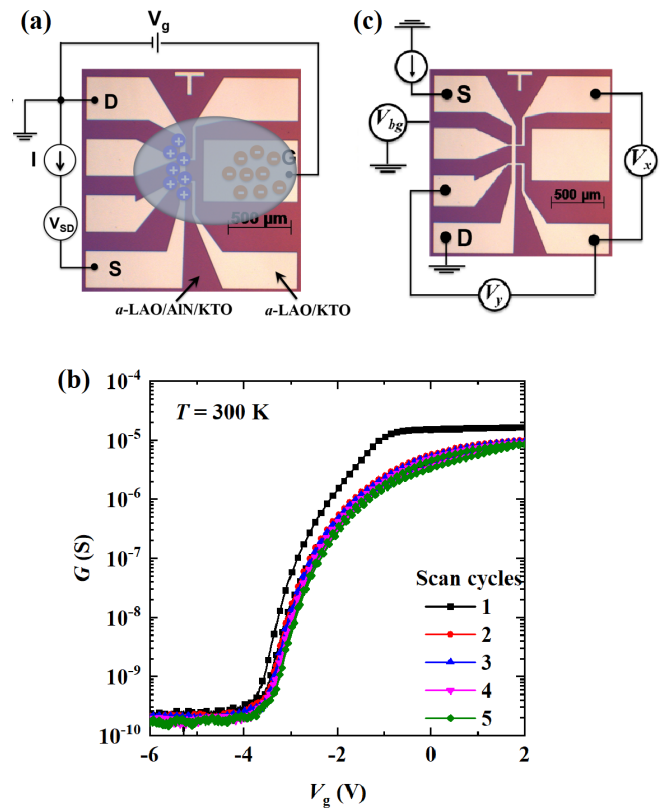


FIG. 1. (a) Optical microscopy image of the Hall bar patterned *a*-LAO/KTO device, including the gate (G), drain (D), and source (S) electrodes, the ionic liquid (IL) drop, and the electrical circuit used to bias and measure the device. (b) Two-probe conductance ($G = I_{\text{SD}}/V_{\text{SD}}$) of the device-1 as a function of the IL gate voltage (V_g) calculated from the measured current while applying a source-drain voltage (V_{SD}). The device switches from a high-conductance to a low-conductance state when varying V_g from positive to negative values. (c) Transport measurement scheme after the IL gating process. The back-gate voltage V_{bg} was applied across the KTO substrate.

cies [23–26]. After scanning for a few cycles, the gate sweep was stopped at $V_g = 0 \text{ V}$, where the device remains stable even after the IL was cleaned off. The device was then cooled down to 2 K leaving a conducting channel at the *a*-LAO/KTO interface with carrier density $n_H \sim 10^{13} \text{ cm}^{-2}$ and mobility, $\mu_H \sim 10^4 \text{ cm}^2\text{V}^{-1}\text{s}^{-1}$, comparable to the values observed in IL-gated crystalline LAO/STO devices [22,27]. The transport measurements in high magnetic fields were carried out a few months after device fabrication and IL gating treatment. The schematic of simultaneous measurements of longitudinal and Hall voltage is displayed in Fig. 1(c). By applying back-gate voltage (V_{bg}) across the KTO substrate, we were able to adjust the electron concentration at the interface.

Figure 2(a) shows the longitudinal resistance, R_{xx} for device-1 measured at different temperatures in a ^3He system while sweeping the magnetic field (B) oriented perpendicular to the interface. Additionally, the Hall resistance data, $R_{xy}(B)$ is displayed in the inset of Fig. 2(a). Device-1 exhibits Hall carrier density $n_H = 1.7 \times 10^{13} \text{ cm}^{-2}$ estimated from a linear fit of $R_{xy}(B)$, and mobility $\mu_H = 5310 \text{ cm}^2\text{V}^{-1}\text{s}^{-1}$. While the carrier density in the IL-gated *a*-LAO/KTO devices

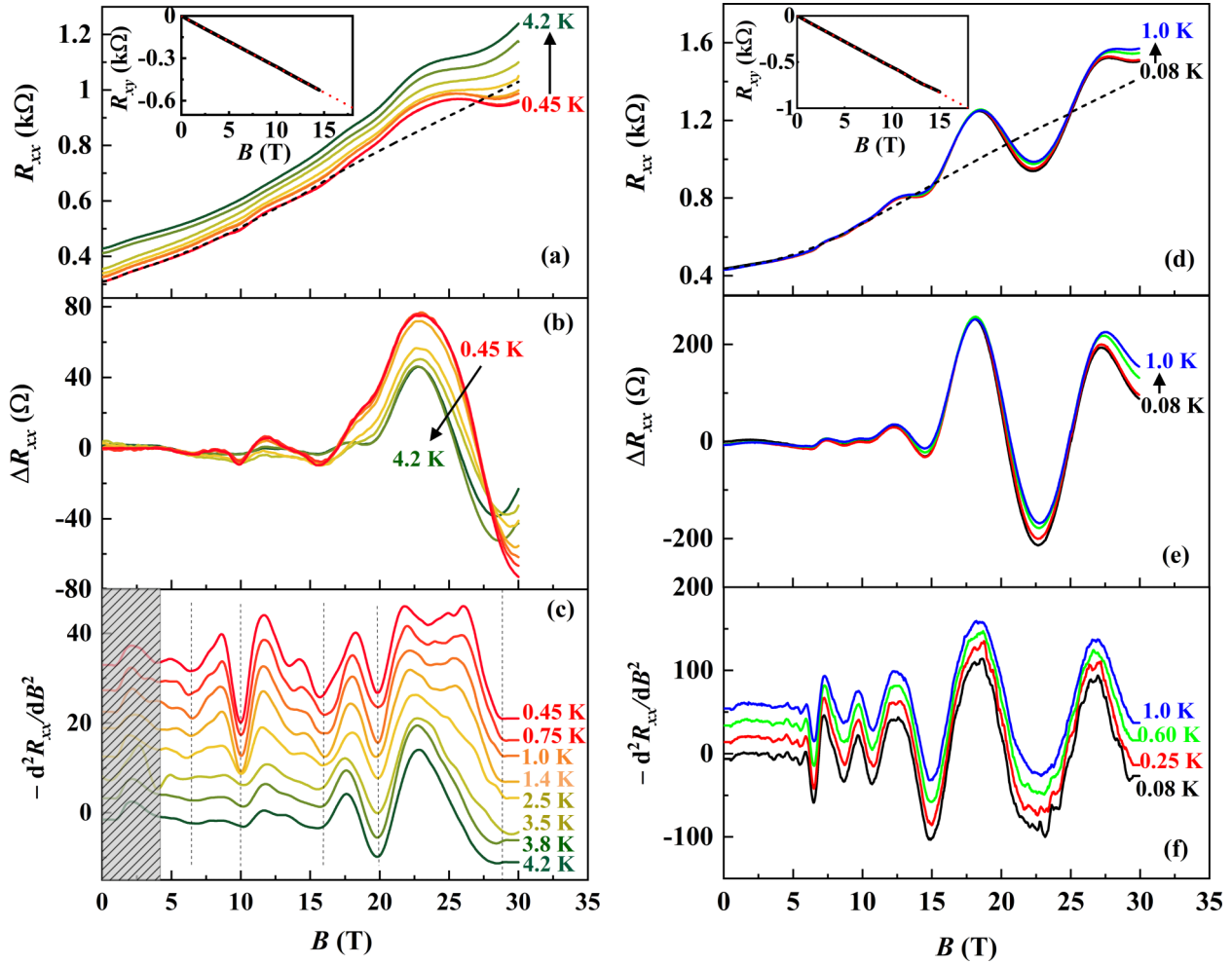


FIG. 2. Observation of quantum oscillations in magnetoresistance of *a*-LAO/KTO devices. Left panels (device-1, $n_H = 1.7 \times 10^{13} \text{ cm}^{-2}$): Magnetic field dependence of transport data at different temperatures (a) longitudinal resistance (R_{xx}), (b) oscillatory resistance (ΔR_{xx}) after subtracting a polynomial background, and (c) the second-order derivative of R_{xx} with respect to B ($-d^2R_{xx}/dB^2$). Right panels (device-2, $n_H = 1.1 \times 10^{13} \text{ cm}^{-2}$): Transport data at different temperatures (d) R_{xx} , (e) ΔR_{xx} , and (f) $-d^2R_{xx}/dB^2$. The dashed lines in (a) and (d) are the nonoscillating background at the lowest temperatures. The $-d^2R_{xx}/dB^2$ vs B curves are shifted along the y axis for clarity. Hall resistance data $R_{xy}(B)$ are shown with linear fit (dashed line) in the insets of (a) device-1 and (d) device-2. The shaded region in Fig. 2(c) covers a temperature-independent rapid increase in $R_{xx}(B)$ in low fields, which is not used in the analysis of SdH oscillations.

remains almost the same over a long period, we noticed a significant drop in the mobility after a few months of IL gating treatment. From Fig. 2(a), a positive magnetoresistance (MR) with clear quantum oscillations superimposed on it is observed. After subtracting a nonoscillating background resistance (dashed line in Fig. 2(a) for $T = 0.45 \text{ K}$) from the $R_{xx}(B)$ data, $\Delta R_{xx}(B)$ is shown in Fig. 2(b). The oscillations start developing at $\sim 4 \text{ T}$ and, as expected, their amplitude increases with decreasing temperature and increasing magnetic field. For a clearer picture of these oscillations, we also show the second-order derivative of R_{xx} ($-d^2R_{xx}/dB^2$) as a function of B in Fig. 2(c). The $-d^2R_{xx}/dB^2(B)$ curve at 4.2 K shows few oscillations, whereas more oscillations pop up when lowering the temperature. This effect originates from the quantization of the density of states of a spin-split band or multiple subbands.

To further resolve these oscillations, we have measured device-2 with $n_H = 1.1 \times 10^{13} \text{ cm}^{-2}$ and $\mu_H = 5800 \text{ cm}^2\text{V}^{-1}\text{s}^{-1}$ in a dilution refrigerator at temperatures down

to 80 mK . $R_{xx}(B)$ and $\Delta R_{xx}(B)$ at different temperatures are shown in Figs. 2(d) and 2(e), respectively. Due to the higher mobility and lower temperatures, more resolved and larger amplitude oscillations are observed for device-2, which start developing from $B \sim 3 \text{ T}$ as revealed by the $-d^2R_{xx}/dB^2$ data shown in Fig. 2(f). Additionally, high-frequency (HF) and small-amplitude oscillations are superimposed on usual low-frequency and large-amplitude oscillations at $T = 80 \text{ mK}$ and 300 mK , which will be discussed in detail later.

In addition to the data shown in the left panels of Fig. 2, device-1 was measured at different tilt angles ranging from 0° to 90° at a base temperature of 400 mK in the ^3He system. The tilt angle θ , as illustrated in the schematic in Fig. 3(a), is measured between the magnetic field B and the normal to the interface. For the in-plane field orientation ($\theta = 90^\circ$), B is parallel to the current. Figures 3(a) and 3(b) show $R_{xx}(B)$ and $R_{xy}(B)$, respectively, measured while varying the field in positive direction. To confirm the data-symmetry, the measurements for $\theta = 0^\circ$ and 90° were also carried out in negative

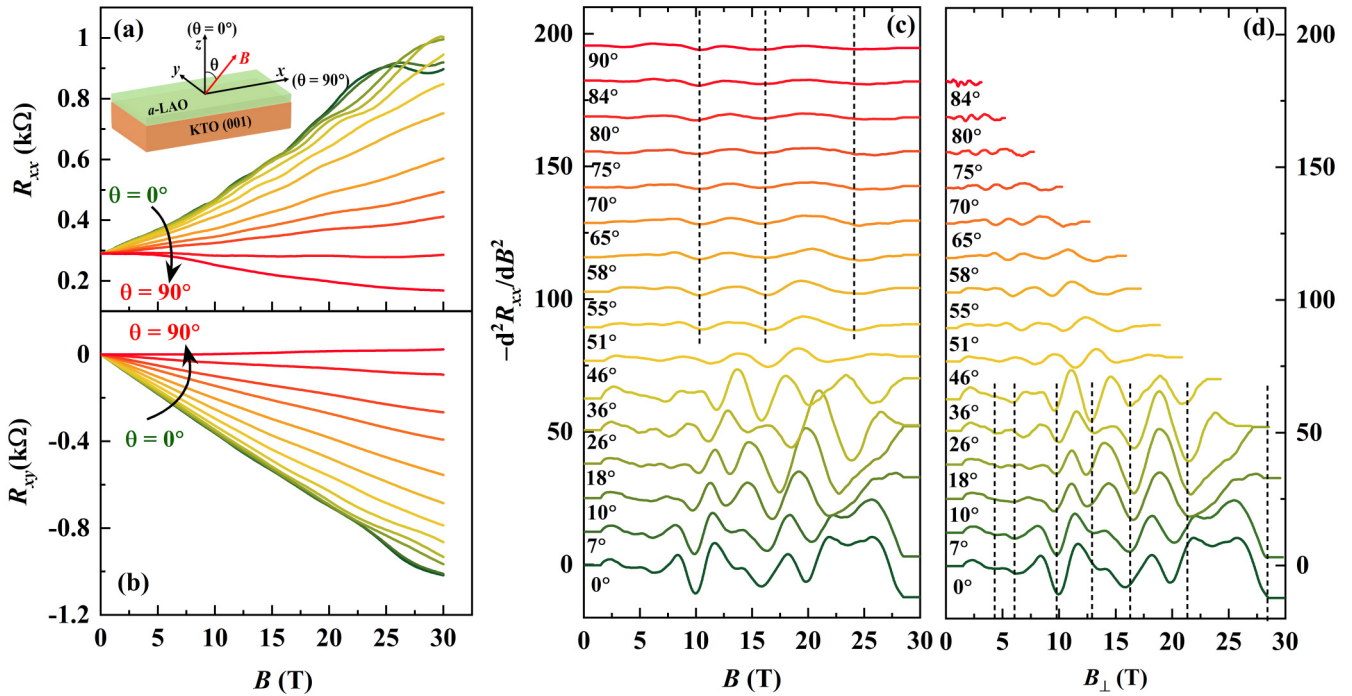


FIG. 3. Angular dependence of the quantum oscillations in device-1. (a) R_{xx} and (b) R_{xy} as a function of magnetic field for different angles $\theta = 0^\circ \rightarrow 90^\circ$ at a temperature $T = 400$ mK. θ is the angle between the normal to KTO (001) plane and the magnetic field direction as depicted in the inset of panel (a). Quantum oscillations in $R_{xx}(B)$ visualized in $-d^2R_{xx}/dB^2$ as a function of (c) the total magnetic field B and (d) the perpendicular field component $B_\perp = B\cos\theta$, respectively. The curves are shifted along the y axis for clarity. The vertical dashed lines mark oscillation minima as a guide to the eyes. The evolution of oscillations with tilt angles indicates the coexistence of 2D and 3D electronic states at the ionic liquid gated a -LAO/KTO interface.

field directions. As shown in the Fig. S1 of Ref. [28], $R_{xy}(B)$ for $\theta = 0^\circ$ is nearly symmetric with respect to zero field. However, $R_{xx}(B)$ exhibits a weak background asymmetry which indicates an inhomogeneous distribution of electrons without affecting the SdH oscillations. We observed a large anisotropic behavior of $R_{xx}(B)$ with varying θ . The positive MR decays with increasing θ and switches to negative MR at high tilt angles. Interestingly, a large and nonsaturating negative MR ($\sim -40\%$ at $B = 30$ T) is perceived for $\theta = 90^\circ$. Such a negative in-plane MR strongly dependent on temperature and carrier density has also been reported for the 2DEG at the LAO/STO interface [29–32] and has been attributed to spin-dependent scattering. The strong spin-orbit interaction (~ 0.47 eV) [11,13] accompanied with spin-disorder scattering then accounts for a large negative MR in the 2DEG at the a -LAO/KTO interface.

To evaluate the dimensionality of the electronic states at the interface, we have examined the angular dependence of the SdH oscillations. Figure 3(c) shows the oscillations for different tilt angles displayed in the second-order derivative of $R_{xx}(B)$. The oscillations show a complex angle dependent evolution which can be attributed to the presence of several electronic subbands [33]. For low tilt angles, $\theta = 0^\circ, \dots, 36^\circ$, most of the oscillation minima progressively shift to higher magnetic fields. More specifically, their position depends on the perpendicular field component $B_\perp (= B\cos\theta)$ only, see Fig. 3(d), which indicates the 2D confinement of conduction electrons at the interface. A slight mismatch in the $\cos\theta$ scaling and the complex evolution of the oscillations' amplitude

with θ (appearance and disappearance of some oscillations which are clearly visible in the FFT analysis [28]) most-likely results from the anticrossing of Landau levels from neighboring 2D subbands. Overall, the 2D oscillations' amplitude decreases with tilt angle and almost vanishes for $\theta = 46^\circ$. For large tilt angles, the parallel field couples to the orbital motion of electrons, therefore enhancing intersubband scattering in the quasi-2D electron system. The enhancement in scattering rate generates additional Landau-level broadening and subsequently suppresses the oscillations' amplitude. In addition, as depicted by the dashed lines in Fig. 3(c), the small-amplitude oscillations which are still visible at higher angles do not depend on the tilt angle, i.e., they scale with the total magnetic field. This observation suggests the existence of an additional 3D conduction channel parallel to the 2D channels at the interface.

To characterize the nature of the observed subbands in more detail, the SdH oscillations for device-1 at different temperatures are analyzed for three specific angles $\theta = 0^\circ, 46^\circ$, and 90° in Fig. 4. In the left panels, Figs. 4(a)–4(c), we show the SdH oscillations as a function of the inverse magnetic field for the three different tilt angles. The corresponding fast Fourier transforms (FFTs) are then displayed in the middle panels, Figs. 4(d)–4(f). We can observe four main frequencies— $f_1 = 25$ T, $f_2 = 42$ T, $f_3 = 64$ T, and $f_4 = 124$ T—in the FFT spectra at $\theta = 0^\circ$ corresponding to four electronic subbands. The total 2D carrier density can be estimated from these frequencies as $n_{\text{SdH}}^{2\text{D}} = 2 \frac{e}{h} \sum_i f_i$, where the factor 2 allows for the spin degeneracy. Using the above frequency

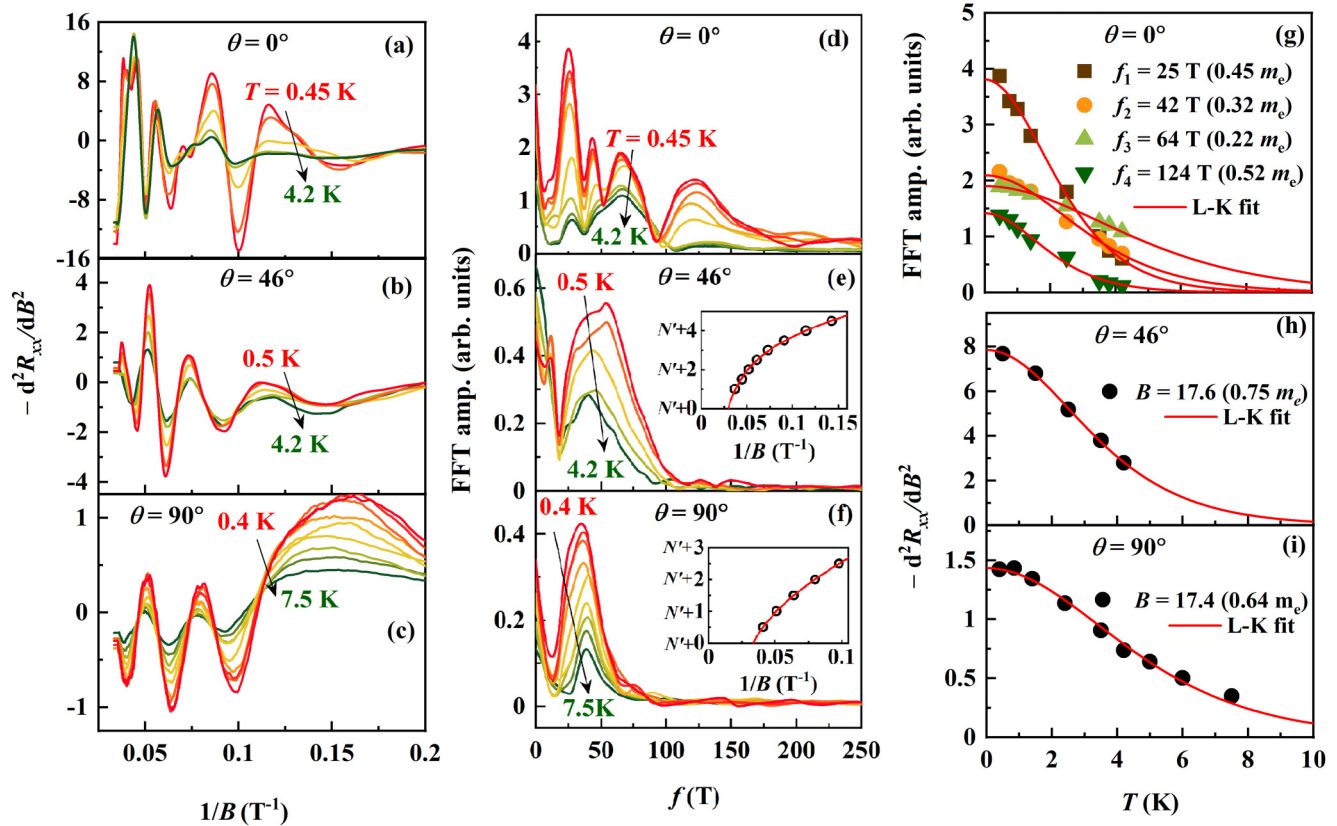


FIG. 4. Oscillations' frequency and cyclotron mass analysis for device-1. Left column: inverse field dependence of the second-order derivative of R_{xx} ($-d^2R_{xx}/dB^2$) at various temperatures and in different device's orientations (a) $\theta = 0^\circ$, (b) $\theta = 46^\circ$, and (c) $\theta = 90^\circ$. The broad oscillation in the low-field regime for $\theta = 90^\circ$ should not be counted as a SdH oscillation since it develops from an abrupt change in the negative MR around ~ 6 T. Middle column: fast Fourier transform (FFT) analysis of $-d^2R_{xx}/dB^2$ versus $1/B$ data shown in the left column. FFT amplitude as a function of frequency for (d) $\theta = 0^\circ$, (e) $\theta = 46^\circ$, and (f) $\theta = 90^\circ$. Insets in panels (e) and (f) show the Landau plots (Landau-level index (N) versus $1/B$) where maxima and minima of oscillations are assigned to the integer and half-integer indices, respectively, and N' is an integer offset. Right column: (g) FFT amplitude as a function of temperature fitted with L-K equation for $\theta = 0^\circ$. The peak-to-valley difference for a given oscillations' period versus temperature, T plots fitted with L-K equation for (h) $\theta = 46^\circ$ and (i) $\theta = 90^\circ$. Symbols are the experimental data and solid-lines are the L-K fit. To avoid a crowded and unclear picture, we show oscillations only for a few selected temperatures in (a); however, the FFT analysis for all temperatures is displayed in (d).

values, we find $n_{\text{SdH}}^{2\text{D}} \approx 1.2 \times 10^{13} \text{ cm}^{-2}$, slightly lower than the n_H ($1.7 \times 10^{13} \text{ cm}^{-2}$) for this device.

In comparison to $\theta = 0^\circ$, fewer oscillations are observed for $\theta = 46^\circ$ and 90° in the full field range, see Figs. 4(b) and 4(c), and the FFT spectrum is dominated by a single broad peak at $f \approx 38$ T. The single broad peak in FFT is manifested from non $1/B$ -periodic oscillations which frequency monotonically increases with magnetic field. The Landau plots (Landau-level index versus $1/B$) displayed in the inset of Figs. 4(e) and 4(f) specify $1/B$ -aperiodic oscillations, similar to that observed in the 2DEG in LAO/STO [30,34] and δ -doped STO [35]. As mentioned above, these oscillations originate from a single 3D band in which the chemical potential or charge carrier density varies as the magnetic field increases [34]. The aperiodicity in the oscillations may exist for $\theta = 0^\circ$ as well, but a similar analysis would become too complex due to the superposition of oscillations of multiple frequencies.

Assuming a spherical Fermi surface, the average 3D carrier density can then be estimated from the SdH frequency f as $n_{\text{SdH}}^{3\text{D}} = \frac{8}{3\sqrt{\pi}} \left(\frac{ef}{h}\right)^{3/2} = 1.3 \times 10^{18} \text{ cm}^{-3}$.

We extract the effective thickness of 3D conduction channel, $t_{3\text{D}}$ by comparing the $n_{\text{SdH}}^{3\text{D}}$ and 3D Hall carrier density, $n_H^{3\text{D}}$. As the $n_{\text{SdH}}^{2\text{D}}$ is a fraction of total carrier density ($n_H = 1.7 \times 10^{13} \text{ cm}^{-2}$), the remaining carriers ($n_H - n_{\text{SdH}}^{2\text{D}} = 5 \times 10^{12} \text{ cm}^{-2}$) would be participating in the 3D oscillations. We calculate $t_{3\text{D}} \approx 40$ nm as $n_H^{3\text{D}} = \frac{n_H - n_{\text{SdH}}^{2\text{D}}}{t_{3\text{D}}} = n_{\text{SdH}}^{3\text{D}}$.

Having established that a majority of electrons are confined at the interface, we now focus on cyclotron mass, m_c analysis. To estimate the m_c values, a fit of the temperature-dependent oscillations' amplitude to the standard Lifshitz-Kosevich (L-K) formula is employed [36]. However, for multiple subbands systems in which oscillations of various frequencies are observed, the m_c evaluated from the FFT amplitude is more reliable. Figure 4(g) shows temperature dependence of FFT amplitude fitted with L-K formula

$$A(T) = A_0 \frac{2\pi^2 k_B m_c T / \hbar e B_{\text{eff}}}{\sinh(2\pi^2 k_B m_c T / \hbar e B_{\text{eff}})}, \quad (1)$$

$$\text{where } \frac{1}{B_{\text{eff}}} = \frac{1}{B_{\text{min}}} + \frac{1}{B_{\text{max}}}.$$

The best fitting yields the m_c values, $0.45 m_e$ (25 T), $0.32 m_e$ (42 T), $0.22 m_e$ (64 T) and $0.52 m_e$ (124 T), lower than those for 2DEG at LAO/STO interface [33]. A large error in the m_c could be expected since a relatively large field window (5–30 T) is used in FFT analysis. We estimate up to 12% error from the ΔR_{xx} data simulated in the same field range using comparable values of frequencies and m_c [28]. Because the oscillations for $\theta = 46^\circ$ and 90° originate from a single band, the m_c is calculated using the peak-to-valley difference for a given oscillations period. The fitted m_c values, $0.75 \pm 0.05 m_e$ for $\theta = 46^\circ$ and $0.64 \pm 0.06 m_e$ for 90° , yield an average $m_c \approx 0.7 m_e$ for the electrons in the 3D band.

To add further validation on the value of the 2D subbands in *a*-LAO/KTO interface, the quantum oscillations observed for device-2 in a perpendicular field orientation (right panel in Fig. 2) are analyzed. Additionally, another experiment was carried out in pulsed magnetic field to extend the magnetic field range up to 55 T. The inset of Fig. 5(b) shows the $R_{xx}(B)$ data measured in the pulsed-field at $T = 500$ mK. The inverse field dependence of the oscillations for dc and pulsed fields are shown in the main panel of Figs. 5(a) and 5(b), respectively. The results in the pulsed-field are similar to the dc-field data, although a higher current (leading to higher effective temperature) leads to a loss of resolution. Figure 5(c) compares the FFT analysis of oscillations in dc and pulsed fields, where the two frequencies $f = 35$ T and 43 T resolved in dc-field measurements merge into one single broad FFT component at $f = 42$ T when measured in pulsed magnetic field. Compared to device-1, the extra FFT peak at $f = 35$ T observed for device-2 is most likely due to its higher mobility. This additional frequency may originate from 3D charge carriers since its value is closed to the 3D oscillation's FFT component ($f = 38$ T) observed for device-1. We assume that 3D oscillations, which have a much smaller amplitude than their 2D counterparts [comparing Figs. 4(a) and 4(c)], were not visible for device-1 when measured in the perpendicular field orientation, but they are well resolved in the device-2. Interestingly, the total carrier density $n_{\text{SdH}}^{2\text{D}} = 1.15 \times 10^{13} \text{ cm}^{-2}$ estimated from five frequencies of SdH oscillations for device-2 is comparable to its Hall carrier density $n_H = 1.1 \times 10^{13} \text{ cm}^{-2}$.

From the analysis of quantum oscillations for both devices, we conclude the occupancy of four 2D subbands at the *a*-LAO/KTO interface. To understand the nature of these subbands, we start from the electronic band structure of bulk KTO where the spin-orbit coupling leads to strong hybridization of Ta: d_{xy} , d_{xz} and d_{yz} orbitals and generates light and heavy mass subbands. Introducing a two-dimensional confinement at KTO-based interfaces induces further splitting of the subbands, i.e., the eigenstates of a quantum well. Additionally, the combination of spin-orbit coupling and 2D confinement in a KTO-based 2DEG reconstruct the orbital symmetries of 2D subbands and renormalize their effective masses to $0.25 m_e$ (light subband) and $0.5 m_e$ (heavy subband) [19]. And, indeed, ARPES performed on a 2DEG at the KTO surface confirms the light and heavy subbands of masses comparable with those predicted theoretically [19,20]. Interestingly, our cyclotron mass analysis on 2D oscillations is also in good agreement with theoretical calculations and suggests the occupancy of two light ($m^* \sim 0.3 m_e$) and two heavy ($m^* \sim 0.5 m_e$) subbands. Moreover, the mass ($\approx 0.7 m_e$) estimated for the 3D

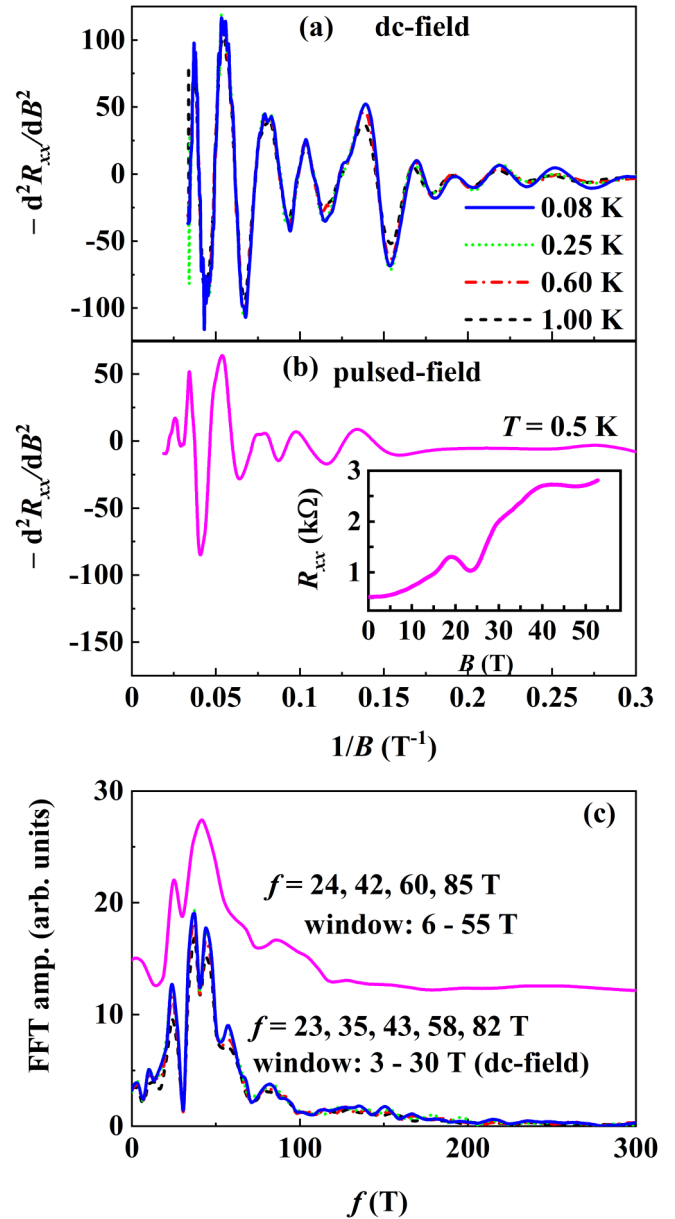


FIG. 5. Analysis of SdH oscillations for device-2 measured in dc ($B = 0$ –30 T) and pulsed fields ($B = 0$ –55 T) applied perpendicular to the interface. Main panels: Inverse field dependence of the second order derivative of the R_{xx} ($-d^2R_{xx}/dB^2$) in (a) dc field and (b) pulsed field. Inset of panel (b) displays the R_{xx} as a function of magnetic field. (c) A comparison of the FFT analysis in different windows of dc-field (3–30 T) and pulsed field (6–55 T). The FFT plot for pulsed-field is shifted along the y axis for better comparison.

band is in very good agreement with the mass of the heavy subband of bulk KTO [19].

Employing the triangular-wedge model [19,33,37] and the subband structure constructed from the analysis of quantum oscillations [28], we estimate the thickness $d \approx 5$ nm of the confined 2DEG at the *a*-LAO/KTO interface. It is important to note that the magnetic length l_B at 30 T becomes comparable to the estimated 2DEG thickness. Therefore, the deformation in the 2D oscillations due to the parallel-field-induced variation of the electron spectrum is

expected at large parallel fields. However, since the 2D oscillations almost disappear at 46° , we were not able to examine the parallel-field effect on the 2D oscillations in more detail.

The high magnetic field may also redistribute the carriers among the Landau levels originating from different subbands and, subsequently, affect the 2D oscillations. Using a simple model based on Landau-level calculations and Lifshitz-Kosevich theory [28], we, however, can exclude any significant change in the positions of the oscillations extrema. Furthermore, we emphasize that despite high magnetic fields and low temperatures, the oscillations from the spin-splitting subbands are not resolved in our measurements, most likely because of the Landau-level broadening exceeding the relatively small Zeeman splitting of a few meV.

Finally, we add a remark on another interesting observation mentioned earlier, the observation of HF oscillations in device-2 at very low temperatures [Fig. 2(f)]. These oscillations are also investigated at different back-gate voltage, V_{bg} applied through the KTO substrate at $T = 80$ mK. The variation in $R_{xx}(B)$ at different V_{bg} , $+35$ V \rightarrow -23 V, is displayed in Fig. 6(a). The evolution of quantum oscillations with V_{bg} is well-visible in $R_{xx}(B)$ curves and clearer in the oscillations spectra plotted as $-d^2R_{xx}/dB^2(B)$ in Fig. 6(b). As expected, the SdH oscillations shift to lower field when V_{bg} varies from $+35$ V to -23 V. Surprisingly, the HF oscillations' amplitude grows rapidly with increasing value of negative V_{bg} . Although the deep analysis of HF oscillations is beyond the scope of this paper, we examine the characteristic of these oscillations in brief. Interestingly, the HF oscillations are reproducible at different temperatures and field sweep rates [28]. We noticed the HF oscillations are not periodic in $1/B$ nor in B . The amplitude of oscillations, which is lower than the conductance quantum ($G_0 = 2e^2/h = 0.77 \mu\text{S}$) at 80 mK and $V_g = -20$ V, decays with increasing temperature [28]. Most likely, these aperiodic and reproducible HF oscillations are resistance fluctuations originating from the quantum-interference of electron transport. Depopulating the electrons at the a -LAO/KTO interface could lead to inhomogeneous 2DEG and form incoherent conductance channels. Such quantum interference phenomena have also been observed in the patterned 2DEG at the STO surface [38] and the LAO/STO interface [39].

IV. SUMMARY

In summary, we have investigated transport properties of the ionic-liquid gated a -LAO/KTO interface in high magnetic fields and at low temperatures. The SdH oscillations measured for low tilt angles reveal the two-dimensional nature of the electron gas at the interface. Additionally, the angle-independent oscillations observed in high tilt angles indicate the coexistence of a 3D conduction channel of width $t_{3D} \sim 40$ nm. Observation of multiple frequencies of 2D oscillations confirms the occupancy of multiple subbands with light and heavy electrons, in good agreement with ARPES and theoretical calculations for KTO-based 2DEG. The single-frequency 3D oscillations yield the effective mass of $\sim 0.7m_e$ corresponding to the heavy band. Furthermore, small-amplitude and high-frequency oscillations superimpos-

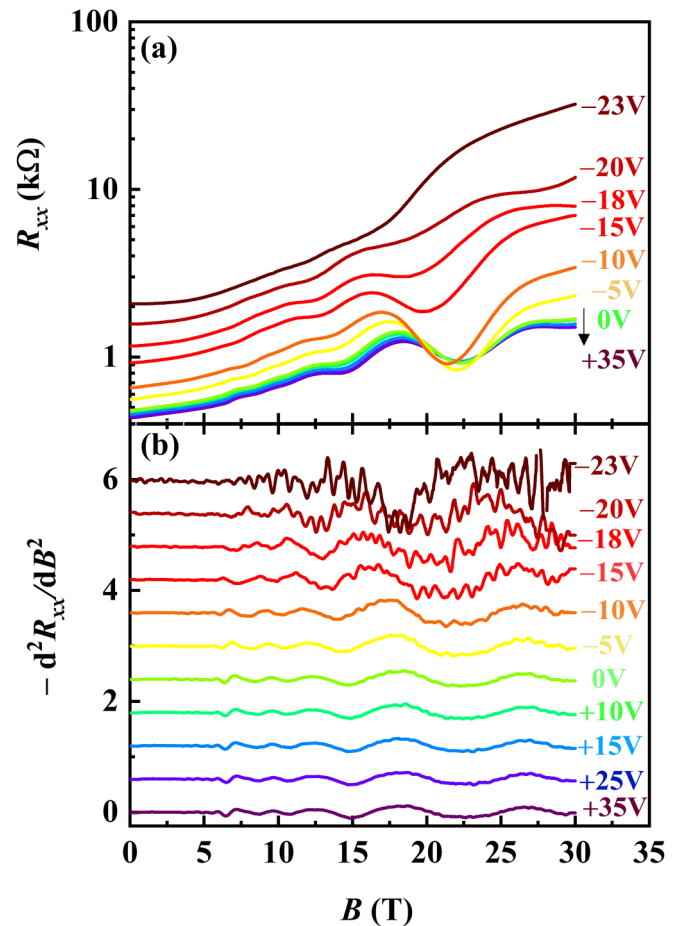


FIG. 6. Evolution of quantum oscillations with back-gate voltage (V_{bg}) for device-2. Magnetic field dependence of (a) R_{xx} and (b) $-d^2R_{xx}/dB^2$ for different V_{bg} and at $T = 80$ mK. The vertical-axis scale in (b) is divided by 1000 and the oscillations spectra are vertically shifted for clarity for $V_g < +35$ V. High-frequency oscillations superimposing the low-frequency SdH oscillations are clearly observed for negative values of V_{bg} .

ing the low-frequency SdH oscillations emerge in the low carrier-density regime. Apart from fine observation of the electronic properties of the KTO-2DEG, this study demonstrates a possible route of studying quantum transport in 2DEG based on 5d-oxides for which creating an epitaxial heterointerface and thereby attaining the high-mobility electron gas is difficult.

ACKNOWLEDGMENTS

We thank Alix McCollam for valuable discussion. We acknowledge the support of HFML-RU/FOM and LNCMI-CNRS, members of the European Magnetic Field Laboratory (EMFL). This study has been partially supported through the EUR grant NanoX Grant No. ANR-17-EURE-0009 in the framework of the ‘‘Programme des Investissements d’Avenir.’’ The work at NUS is supported by the Agency for Science, Technology, and Research (A*STAR) under its Advanced Manufacturing and Engineering (AME) Individual Research Grant (IRG) (No. A1983c0034), the National University of

Singapore (NUS) Academic Research Fund (AcRF Tier 1 Grant No. R-144-000-391-114), and the Singapore National

Research Foundation (NRF) under the Competitive Research Programs (CRP Grant No. NRF-CRP15-2015-01).

- [1] H. Y. Hwang, Y. Iwasa, M. Kawasaki, B. Keimer, N. Nagaosa, and Y. Tokura, Emergent phenomena at oxide interfaces, *Nat. Mater.* **11**, 103 (2012).
- [2] S. Stemmer and S. James Allen, Two-dimensional electron gases at complex oxide interfaces, *Annu. Rev. Mater. Res.* **44**, 151 (2014).
- [3] Z. Huang, X. Renshaw Wang, A. Rusydi, J. Chen, H. Yang, and T. Venkatesan, Interface engineering and emergent phenomena in oxide heterostructures, *Adv. Mater.* **30**, 1802439 (2018).
- [4] P. Noël, F. Trier, L. M. V. Arche, J. Bréhin, D. C. Vaz, V. Garcia, S. Fusil, A. Barthélémy, L. Vila, M. Bibes *et al.*, Nonvolatile electric control of spin-charge conversion in a SrTiO₃ Rashba system, *Nature (London)* **580**, 483 (2020).
- [5] A. Ohtomo and H. Hwang, A high-mobility electron gas at the LaAlO₃/SrTiO₃ heterointerface, *Nature (London)* **427**, 423 (2004).
- [6] A. D. Caviglia, M. Gabay, S. Gariglio, N. Reyren, C. Cancellieri, and J.-M. Triscone, Tunable Rashba Spin-Orbit Interaction at Oxide Interfaces, *Phys. Rev. Lett.* **104**, 126803 (2010).
- [7] C. Yin, P. Seiler, L. M. K. Tang, I. Leermakers, N. Lebedev, U. Zeitler, and J. Aarts, Tuning Rashba spin-orbit coupling at LaAlO₃/SrTiO₃ interfaces by band filling, *Phys. Rev. B* **101**, 245114 (2020).
- [8] L. Li, C. Richter, J. Mannhart, and R. Ashoori, Coexistence of magnetic order and two-dimensional superconductivity at LaAlO₃/SrTiO₃ interfaces, *Nat. Phys.* **7**, 762 (2011).
- [9] J. A. Bert, B. Kalisky, C. Bell, M. Kim, Y. Hikita, H. Y. Hwang, and K. A. Moler, Direct imaging of the coexistence of ferromagnetism and superconductivity at the LaAlO₃/SrTiO₃ interface, *Nat. Phys.* **7**, 767 (2011).
- [10] K. Zou, S. Ismail-Beigi, K. Kisslinger, X. Shen, D. Su, F. J. Walker, and C. H. Ahn, LaTiO₃/KTaO₃ interfaces: A new two-dimensional electron gas system, *APL Mater.* **3**, 036104 (2015).
- [11] H. Zhang, H. Zhang, X. Yan, X. Zhang, Q. Zhang, J. Zhang, F. Han, L. Gu, B. Liu, Y. Chen *et al.*, Highly mobile two-dimensional electron gases with a strong gating effect at the amorphous LaAlO₃/KTaO₃ interface, *ACS Appl. Mater. Interfaces* **9**, 36456 (2017).
- [12] H. Zhang, Y. Yun, X. Zhang, H. Zhang, Y. Ma, X. Yan, F. Wang, G. Li, R. Li, T. Khan *et al.*, High-Mobility Spin-Polarized Two-Dimensional Electron Gases at EuO/KTaO₃ Interfaces, *Phys. Rev. Lett.* **121**, 116803 (2018).
- [13] N. Wadehra, R. Tomar, R. M. Varma, R. Gopal, Y. Singh, S. Dattagupta, and S. Chakraverty, Planar Hall effect and anisotropic magnetoresistance in polar-polar interface of LaVO₃-KTaO₃ with strong spin-orbit coupling, *Nat. Commun.* **11**, 874 (2020).
- [14] K. Ueno, S. Nakamura, H. Shimotani, H. Yuan, N. Kimura, T. Nojima, H. Aoki, Y. Iwasa, and M. Kawasaki, Discovery of superconductivity in KTaO₃ by electrostatic carrier doping, *Nat. Nanotechnol.* **6**, 408 (2011).
- [15] C. Liu, X. Yan, D. Jin, Y. Ma, H.-W. Hsiao, Y. Lin, T. M. Bretz-Sullivan, X. Zhou, J. Pearson, B. Fisher *et al.*, Two-dimensional superconductivity and anisotropic transport at KTaO₃ (111) interfaces, *Science* **371**, 716 (2021).
- [16] Z. Chen, Z. Liu, Y. Sun, X. Chen, Y. Liu, H. Zhang, H. Li, M. Zhang, S. Hong, T. Ren *et al.*, Two-Dimensional Superconductivity at the LaAlO₃/KTaO₃ (110) Heterointerface, *Phys. Rev. Lett.* **126**, 026802 (2021).
- [17] V. R. Cooper, Enhanced carrier mobilities in two-dimensional electron gases at III-III/V oxide heterostructure interfaces, *Phys. Rev. B* **85**, 235109 (2012).
- [18] Y. Wang, W. Tang, J. Cheng, M. Behtash, and K. Yang, Creating two-dimensional electron gas in polar/polar perovskite oxide heterostructures: First-principles characterization of LaAlO₃/A⁺B⁵⁺O₃, *ACS Appl. Mater. Interfaces* **8**, 13659 (2016).
- [19] A. F. Santander-Syro, C. Bareille, F. Fortuna, O. Copie, M. Gabay, F. Bertran, A. Taleb-Ibrahimi, P. Le Fèvre, G. Herranz, N. Reyren, M. Bibes, A. Barthélémy, P. Lecoeur, J. Guevara, and M. J. Rozenberg, Orbital symmetry reconstruction and strong mass renormalization in the two-dimensional electron gas at the surface of KTaO₃, *Phys. Rev. B* **86**, 121107(R) (2012).
- [20] P. D. C. King, R. H. He, T. Eknapakul, P. Buaphet, S.-K. Mo, Y. Kaneko, S. Harashima, Y. Hikita, M. S. Bahramy, C. Bell, Z. Hussain, Y. Tokura, Z.-X. Shen, H. Y. Hwang, F. Baumberger, and W. Meevasana, Subband Structure of a Two-Dimensional Electron Gas Formed at the Polar Surface of the Strong Spin-Orbit Perovskite KTaO₃, *Phys. Rev. Lett.* **108**, 117602 (2012).
- [21] S. Harashima, C. Bell, M. Kim, T. Yajima, Y. Hikita, and H. Y. Hwang, Coexistence of two-dimensional and three-dimensional Shubnikov-de Haas oscillations in Ar⁺-irradiated KTaO₃, *Phys. Rev. B* **88**, 085102 (2013).
- [22] S. Zeng, W. Lu, Z. Huang, Z. Liu, K. Han, K. Gopinadhan, C. Li, R. Guo, W. Zhou, H. H. Ma *et al.*, Liquid-gated high mobility and quantum oscillation of the two-dimensional electron gas at an oxide interface, *ACS Nano* **10**, 4532 (2016).
- [23] S. W. Zeng, X. M. Yin, T. S. Heng, K. Han, Z. Huang, L. C. Zhang, C. J. Li, W. X. Zhou, D. Y. Wan, P. Yang, J. Ding, A. T. S. Wee, J. M. D. Coey, T. Venkatesan, A. Rusydi, and A. Ariando, Oxygen Electromigration and Energy Band Reconstruction Induced by Electrolyte Field Effect at Oxide Interfaces, *Phys. Rev. Lett.* **121**, 146802 (2018).
- [24] J. Jeong, N. Aetukuri, T. Graf, T. D. Schladt, M. G. Samant, and S. S. P. Parkin, Suppression of metal-insulator transition in VO₂ by electric field-induced oxygen vacancy formation, *Science* **339**, 1402 (2013).
- [25] M. Li, W. Han, X. Jiang, J. Jeong, M. G. Samant, and S. S. Parkin, Suppression of ionic liquid gate-induced metallization of SrTiO₃ (001) by oxygen, *Nano Lett.* **13**, 4675 (2013).
- [26] C. Leighton, Electrolyte-based ionic control of functional oxides, *Nat. Mater.* **18**, 13 (2019).

- [27] P. Gallagher, M. Lee, T. A. Petach, S. W. Stanwyck, J. R. Williams, K. Watanabe, T. Taniguchi, and D. Goldhaber-Gordon, A high-mobility electronic system at an electrolyte-gated oxide surface, *Nat. Commun.* **6**, 6437 (2015).
- [28] See Supplemental Material at <http://link.aps.org/supplemental/10.1103/PhysRevResearch.3.033234> for details of the measurements in both positive and negative field directions, FFT analysis of oscillations at small angles, cyclotron mass analysis from the FFT of simulated oscillations, electron confinement at the interface, Landau-levels calculation and Lifshitz-Kosevich model, and high-frequency oscillations.
- [29] M. Diez, A. M. R. V. L. Monteiro, G. Mattoni, E. Cobanera, T. Hyart, E. Mulazimoglu, N. Bovenzi, C. W. J. Beenakker, and A. D. Caviglia, Giant Negative Magnetoresistance Driven by Spin-Orbit Coupling at the $\text{LaAlO}_3/\text{SrTiO}_3$ Interface, *Phys. Rev. Lett.* **115**, 016803 (2015).
- [30] M. Yang, K. Han, O. Torresin, M. Pierre, S. Zeng, Z. Huang, T. V. Venkatesan, M. Goiran, J. M. D. Coey, Ariando, and W. Escoffier, High field magneto-transport in two-dimensional electron gas $\text{LaAlO}_3/\text{SrTiO}_3$, *Appl. Phys. Lett.* **109**, 122106 (2016).
- [31] M. Ben Shalom, C. W. Tai, Y. Lereah, M. Sachs, E. Levy, D. Rakhmilevitch, A. Palevski, and Y. Dagan, Anisotropic magnetotransport at the $\text{SrTiO}_3/\text{LaAlO}_3$ interface, *Phys. Rev. B* **80**, 140403(R) (2009).
- [32] X. Wang, W. M. Lü, A. Annadi, Z. Q. Liu, K. Gopinadhan, S. Dhar, T. Venkatesan, and Ariando, Magnetoresistance of two-dimensional and three-dimensional electron gas in $\text{LaAlO}_3/\text{SrTiO}_3$ heterostructures: Influence of magnetic ordering, interface scattering, and dimensionality, *Phys. Rev. B* **84**, 075312 (2011).
- [33] A. McCollam, S. Wenderich, M. K. Kruize, V. K. Guduru, H. J. A. Molegraaf, M. Huijben, G. Koster, D. H. A. Blank, G. Rijnders, A. Brinkman, H. Hilgenkamp, U. Zeitler, and J. C. Maan, Quantum oscillations and subband properties of the two-dimensional electron gas at the $\text{LaAlO}_3/\text{SrTiO}_3$ interface, *APL Mater.* **2**, 022102 (2014).
- [34] K. Rubi, J. Gosteau, R. Serra, K. Han, S. Zeng, Z. Huang, B. Warot-Fonrose, R. Arras, E. Snoeck, M. Goiran, and W. Escoffier, Aperiodic quantum oscillations in the two-dimensional electron gas at the $\text{LaAlO}_3/\text{SrTiO}_3$ interface, *npj Quant. Mater.* **5**, 9 (2020).
- [35] B. Jalan, S. Stemmer, S. Mack, and S. J. Allen, Two-dimensional electron gas in δ -doped SrTiO_3 , *Phys. Rev. B* **82**, 081103(R) (2010).
- [36] D. Shoenberg, *Magnetic Oscillations in Metals* (Cambridge University Press, Cambridge, UK, 2009).
- [37] A. Santander-Syro, O. Copie, T. Kondo, F. Fortuna, S. Pailhes, R. Weht, X. Qiu, F. Bertran, A. Nicolaou, A. Taleb-Ibrahimi *et al.*, Two-dimensional electron gas with universal subbands at the surface of SrTiO_3 , *Nature (London)* **469**, 189 (2011).
- [38] S. W. Stanwyck, P. Gallagher, J. Williams, and D. Goldhaber-Gordon, Universal conductance fluctuations in electrolyte-gated SrTiO_3 nanostructures, *Appl. Phys. Lett.* **103**, 213504 (2013).
- [39] P. Irvin, H. Lee, J.-W. Lee, M. Briggeman, S. Lu, A. Annadi, G. Cheng, M. Tomczyk, J. Li, M. Huang *et al.*, Strong Aharonov-Bohm quantum interference in simply connected $\text{LaAlO}_3/\text{SrTiO}_3$ structures, *Phys. Rev. B* **100**, 161103(R) (2019).